Different Observations of Sea Surface Wind Pattern Under Deep Convection by Sentinel-1 SARs, Scatterometers, and Radiometers in Collocation

Tran Vu La, *Member, IEEE*, and Christophe Messager

***Abstract*—Strong ocean surface mean and gust winds associated with deep convection can cause significant damages. It is hard to estimate surface convective wind gusts since they may occur suddenly and become intense quickly. This problem is even more challenging for tropical and subtropical regions over which convection is particularly intense while one has little *in situ* and remote sensing data. This article presents the collocation of several low-earth orbit (LEO) acquired data sources to observe and estimate ocean surface convective winds. The LEO devices include Sentinel-1 synthetic aperture radar (SAR), ASCAT-A/B/C scatterometers, Windsat, and SMAP radiometers. This combination enables the short- and long-term observations of ocean wind pattern variabilities, for instance, a mesoscale squall line and a submesoscale wind cell. Sentinel-1 data can offer convective wind gust estimates at a high spatial resolution, whereas the other sources (SMAP, Windsat, and ASCAT-A/B/C) only estimate wind gusts at a scale larger than 0.25° grid. Also, thanks to the LEO data collocation, one can observe the displacement direction of surface wind patterns and their intensity variabilities (15–25 m/s). Surface wind patterns move according to the horizontal displacement of deep convective clouds aloft observed by the Meteosat geostationary satellite. Likewise, the wind intensity variability and deep cloud brightness temperature evolve accordingly. Using simultaneous rainfall and wind speed measurements from Windsat, this study showed that the high-intensity radar backscattering from *C*-band Sentinel-1 SAR data is mainly induced by convective winds rather than precipitation.**

***Index Terms*—ASCAT, convective system (CS), convective wind gust, deep convection, deep convective cloud, downdraft, Meteosat, Sentinel-1, SMAP, Windsat.**

I. Introduction

CONVECTIVE systems (CSs) characterized by cumulonimbus clouds are extreme weather events that frequently occur in the tropical and subtropical zones. Some CS types (e.g., supercell thunderstorms or mesoscale CSs) may be classified as a natural hazard since they can cause significant damages [1]–[4]: strong surface winds (or wind gusts), heavy rainfall, and intense lightning. In particular, they may occur suddenly and become more intense very quickly, and that feature makes the CS observation and prediction more complicated, notably at a high spatial resolution. However, this work has been improved in recent years thanks to a complete network of GEOstationary (GEO) satellites (Meteosat, GOES, Himawari, Gaofen) covering all the earth. Meanwhile, the observation and estimation of strong surface wind speed and intense precipitation associated with CSs are still significant challenges due to the lack of remote sensing and *in situ* data at high spatial and temporal resolutions. Heavy rain may be particularly dangerous for land-use applications since it may cause flash floods, whereas strong wind gusts may significantly damage many onshore, offshore, and coastal activities. Following the previous studies [5]–[9], this article presents a new methodology to estimate surface convective wind gusts over the sea by various satellite data collocation.

The formation of surface wind gusts associated with deep convection can be summarized as follows. The warm air moves upwards and is cooled at a higher altitude. The cooled air then induces air parcels moving downwards, also called downdrafts. In some cases, the convective condition within the mid-atmospheric boundary layer makes downdrafts intense enough to produce wind downburst toward the sea surface. When hitting the sea surface, the intense downdrafts are horizontally deflected and produce local surface winds impacting local and regional horizontal wind variability, as well as triggering strong wind gusts, as discussed in [10]. The more intense downdrafts, the stronger the surface wind intensity may be observed. The damages caused by this event for human life and industrial activities have been reported for a long time in many tropical regions [1]–[4], [11]–[13]. For instance, strong surface winds associated with deep convection are a significant hazard for fishing activities over Lake Victoria, one of the African Great Lakes [1], [2], [11]. Likewise, convective wind gusts cause significant damages for offshore oil/gas exploitation over the Gulf of Guinea and the Gulf of Mexico [12].

Among the tropical zones, the Gulf of Guinea is one of the regions in which the lack of observation and measurement data of convective wind gusts, especially at a small scale, is the most significant. In order to overcome such issues, this article focuses on the combination and collocation of data acquired by various devices such as synthetic aperture radar (SAR), scatterometers,

Manuscript received March 4, 2022; revised April 26, 2022; accepted April 28, 2022. Date of publication May 3, 2022; date of current version May 18, 2022. This work was supported in part by the Center National d'Etudes Spatiales in the framework of the Plateforme d'Exploitation des Produits Sentinel Program and in part by the BPI France. *(Corresponding author: Tran Vu La.)*

Tran Vu La is with B-SPACE, 29200 Brest, France (e-mail: tranvu-laa@yahoo.com).

Christophe Messager is with Extreme Weather Expertises, 29200 Brest, France (e-mail: christophe.messager@exwexs.fr).

Digital Object Identifier 10.1109/JSTARS.2022.3172375

and radiometers. Such a collocation with short and long observation time lags between the devices enables observations of not only the temporal and spatial evolution of surface wind gusts but also to evaluate the accuracy of wind speed estimates. The advantages and limitations of these devices are discussed as follows.

First, La *et al.* [5]–[9] suggested that *C*-band Sentinel-1 SAR could be used to observe and estimate strong surface wind speed (10–25 m/s) associated with deep convection at mesoscales and submesoscales. In particular, these studies indicated a strong relationship between deep convective clouds with low brightness temperatures (BTs) (200–230 K) and surface wind patterns observed on Sentinel-1 images. Both features have almost the same location and close shapes. This assumption was completed in [8] and [9] by the collocation of data acquired by three satellites (Meteosat, Aeolus, and Sentinel-1) to obtain a 3-D view of deep convection, including the observations of deep convective clouds by Meteosat, intense downdrafts at the atmospheric mid-levels by Aeolus Lidar, and strong surface wind patterns over the sea by Sentinel-1. The results in [5]–[9] permit to strengthen the assumption that the high-intensity radar backscattering on Sentinel-1 SAR is associated with surface convective wind gusts rather than induced from precipitation, also as indicated in [14] and [15].

Second, as well as Sentinel-1 SAR, the wind data acquired by scatterometers can be used to observe and estimate strong surface wind speed associated with deep convection. The studies [16], [17] indicated the relationship between surface wind patterns observed by the ASCAT *C*-band scatterometers and deep convective clouds. However, due to the coarse spatial resolution of ASCAT, one could not estimate wind hot spots (higher than 15 m/s wind intensity) associated with the coldest cloud patterns [16]. Despite this inconvenience, the ASCAT-A/B/C data are used in this article to observe mesoscale surface wind patterns thanks to their large swath. In addition, the work in [18]–[20] indicated that the ASCAT data were almost not impacted by precipitation like *C*-band Sentinel-1 SAR.

Third, like the scatterometers, the radiometers can estimate surface wind speed. This article uses data acquired by the Windsat Polarimetric [21], [22] and SMAP radiometers [23], [24] to estimate the strong surface wind speed associated with deep convection. Additionally, Windsat can measure quite accurately rainfall associated with surface wind patterns. This ability will permit observing the relationship between strong surface wind speed and precipitation under deep convection. Furthermore, through the comparison between surface wind patterns (observed by Sentinel-1 *C*-band SAR and Windsat) and rainfall (measured by Windsat), one may answer a debate question about the interpretation of the high-intensity radar backscattering areas observed on the *C*-band SAR images whether it is associated with convective wind gusts or precipitation as assumed by [25] and [26]. In addition to the Windsat radiometer, this article uses data acquired by the SMAP *L*-band radiometer [23], [24] to observe convective wind gusts. Like Windsat, surface wind speed is retrieved from the SMAP BT measurements. However, the *L*-band radar signal is not impacted by precipitation, even under heavy rainfall [14], [23]. Therefore, the surface wind speed estimated by SMAP can be used as a reference to evaluate the impact of rain on surface wind speed retrieval at the other frequencies (above *C*-band). As suggested in [24], the SMAP wind data should be used for moderate wind speed above 12 m/s.

The potential of data acquired from Sentinel-1 SAR, ASCAT scatterometers, and Windsat and SMAP radiometers to estimate and observe the evolution of surface convective wind gusts is actual under the collocation conditions of these datasets. Over the Gulf of Guinea, one can note that Sentinel-1, Windsat, and SMAP have close orbit time for ascending (around 17:00–18:00 UTC) and descending (around 05:00–06:00 UTC) directions. In particular, the period 17:00–18:00 UTC corresponds to the convection peak for this region. Therefore, for some days, one can collocate the Sentinel-1, Windsat, and SMAP data to observe the evolution of surface wind patterns. The observation time lag between three devices in these cases does not exceed 30 min (short term), and this time is relevant to observe the evolution of wind hot spots. The passing time of the ASCAT-A/B/C scatterometers over the Gulf of Guinea is different from that of Sentinel-1, Windsat, and SMAP (up to 2–3 h time lag). However, the collocation of the ASCAT data and the others permits observing the evolution of surface wind patterns for a long time (long term). One should note that some intense mesoscale CSs may exist for several hours [27]. So, through the combination of Sentinel-1, ASCAT-A/B/C, Windsat, and SMAP, this article presents the observations of surface wind pattern evolution for short and long terms, which has not been illustrated yet in the literature.

In addition to the low-earth orbit (LEO) satellites discussed above (Sentinel-1, ASCAT, Windsat, and SMAP), this article uses the Meteosat GEO images (SEVIRI data–0 degree, channel-10-IR 12.0) corresponding to the LEO data to detect deep convective clouds. The Meteosat sampling time of 15 min eases the investigation of the relationship between deep convective clouds and surface wind patterns. The time lag between Meteosat and LEO data is less than 10 min in this article. Likewise, the Meteosat images are resampled on the grid of Sentinel-1 ones to facilitate comparisons.

The rest of this article is organized as follows. Section II presents the methodology of this study, including data preparation, the collocation of LEO data, and the methods of surface wind speed retrieval from LEO data. Section III illustrates the observations of surface wind pattern evolution through the collocation of LEO data for two cases: 1) mesoscale squall and 2) convection cell wind patterns. Section IV discusses the relationship between surface wind patterns and precipitation measured by Windsat. Finally, Section V presents the discussion and conclusion.

II. Methodology

A. Data Preparation and Collocation

Fig. 1 presents the Gulf of Guinea imaged by Sentinel-1, ASCAT-A/B/C, Windsat, and SMAP for descending orbit direction, February 4, 2019 [Fig. 1(a)], and ascending orbit direction, December 19, 2019 [Fig. 1(b)]. In the two cases, the footprints

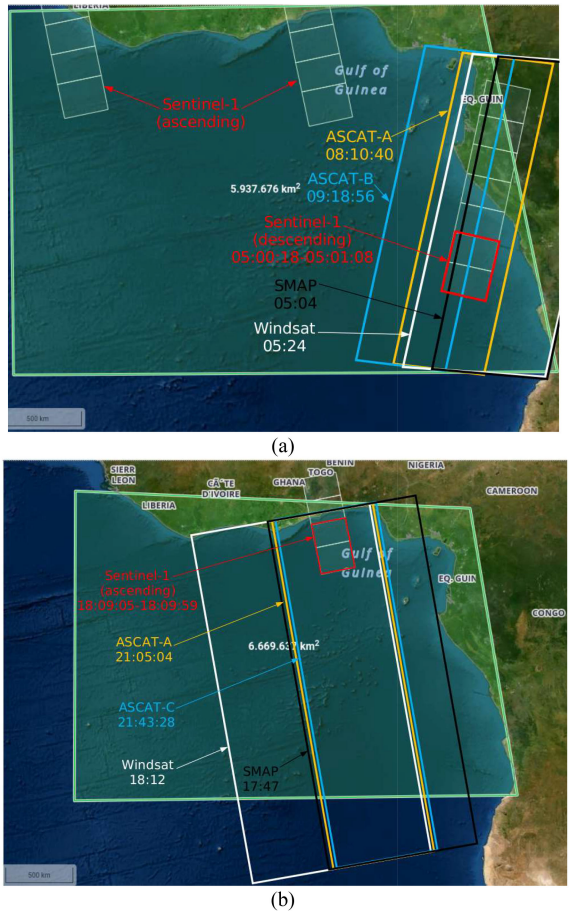

Fig. 1. Gulf of Guinea imaged by Sentinel-1, ASCAT, Windsat, and SMAP LEO satellites for (a) descending orbit direction, February 4, 2019 and (b) ascending orbit direction, December 19, 2019. The Sentinel-1, ASCAT-A, ASCAT-B/C (descending/ascending), Windsat, and SMAP footprints are highlighted in red, yellow, blue, white, and black, respectively.

of the five devices are superposed. Sentinel-1 has the narrowest swath but the highest spatial resolution. The others have a coarse spatial resolution but a large swath. In general, a footprint matching between three or four LEO satellite instruments remains complicated. Based on several footprint matching cases between the five devices indicated, this article presents two cases of descending and ascending orbit directions, as shown in Fig. 1. In both cases, the ASCAT-A/B/C, Windsat, and SMAP data are resampled on the Sentinel-1 grid to facilitate the observation of surface wind patterns. Likewise, the Meteosat data are collocated with the Sentinel-1 data to observe the corresponding locations between deep convective clouds and surface wind patterns.

Table I presents the Sentinel-1, ASCAT-A/B/C, Windsat, and SMAP acquisition time for the descending and ascending cases. In both cases, the observation time lag between Sentinel-1, Windsat, and SMAP is relatively short (below 30 min), whereas the one between ASCAT-A/B/C and the others is about 2–3 h. These differences permit observing the changes of surface wind patterns more clearly, for a short term (below 30 min) and a long one (about 2–3 h). One should note that a CS can exist for several hours, as indicated in [27]. Thanks to the short Meteosat time sampling of 15 min, one can find the corresponding Meteosat

TABLE I
COMBINATION OF LEO AND GEO SATELLITES FOR CS OBSERVATIONS AND SURFACE CONVECTIVE WIND GUST ESTIMATION

Case	Satellite	Acquisition time (UTC)
Descending (february 4, 2019), offshore Angola	Sentinel-1 (100 m)	05:00:18–05:01:08
	Windsat (25 KM)	05:24:00
	SMAP (25 KM)	05:04:00
	ASCAT-A (12.5 KM)	08:10:40
	ASCAT-B (12.5 KM)	09:18:56
	Meteosat (2 km)	04:51:00–09:21:00
Ascending December 19, 2019, offshore Ghana-Togo	Sentinel-1 (100 m)	18:09:05–18:09:59
	Windsat (25 KM)	18:12:00
	SMAP (25 KM)	17:47:00
	ASCAT-A (12.5 KM)	21:05:04
	ASCAT-C (12.5 KM)	21:43:28
	Meteosat (2 km)	17:51:00–21:36:00

images to the data acquired by the five LEO devices. The small-time lag between Meteosat and LEO devices facilitates the observation of the relationship between deep convective clouds and surface wind patterns.

B. Surface Wind Pattern Estimation

Sea surface wind patterns associated with deep convection can be observed and estimated from Sentinel-1 data, as indicated in [5]–[9]. This result is based on the observed link between intense convective downdrafts and the associated strong surface wind speed (or wind gust) when the former hits the sea surface. This strong wind does increase sea surface roughness significantly that can be imaged by the SARs as high-intensity radar backscattering or normalized radar cross section (NRCS). Based on the geophysical model functions, one can retrieve surface wind speed from the observed NRCS. For Sentinel-1 *C*-band SAR data, one uses CMOD5.N [28] to retrieve surface wind speed from the processed NRCS. The CMOD5.N can estimate wind speed up to 25 m/s [29], [30] close to the convective wind intensity reported in [2], [11], [31], and [32]. Thanks to the high spatial resolution and a large swath of Sentinel-1 images, one can observe surface wind patterns at mesoscales and submesoscales.

As well as Sentinel-1, the ASCAT *C*-band scatterometers can image the modulations of sea surface roughness due to surface winds through radar backscattering or NRCS. Therefore, one can retrieve surface wind speed from the NRCS observed by ASCAT using CMOD5.N. This article uses the ASCAT-estimated wind speeds [33] with a 12.5-km grid to estimate surface convective wind gusts. The convective wind hot-spots at a small scale may not be observed by ASCAT, due to their coarse spatial resolution; however, the ASCAT wide swath permits observing mesoscale surface wind patterns and their space changes.

Sea surface wind speed can also be retrieved from the BT measurements using the Windsat and SMAP radiometers [21]–[24]. For that, the differences between the measured BT and that of an idealized flat ocean surface are used as input of a radiative transfer model (RTM). By inverting the RTM, one can obtain surface wind speed estimates. The RTM processes are close to the CMOD5.N function, although the input parameters are different (ocean surface BT versus radar backscattering). The Windsat radiometer operates in five discrete channels (6.8, 10.7,

18.7, 23.8, and 37.0 GHz), and surface wind speed is retrieved from the BT measurements through the five channels. Except for the *C*-band channel (6.8 GHz), the data from the others (*X*-band and *K*-band) are significantly impacted by rain [14], [15], [21]. Therefore, Meissner and Onentz [21] suggested an algorithm to retrieve surface wind speed from the BT measurements under the rain. The accuracy of the wind speed estimates from the rain-free algorithm (also called all-weather 10 m wind speed) is acceptable to observe convective wind gusts. The Windsat rain-free wind data with a 0.25° grid [22] are used in this article. Unlikely Windsat, the BT measurements using the *L*-band SMAP radiometers are not sensitive to precipitation, even heavy rainfall [14], [23]. Therefore, the SMAP-retrieved surface wind speed is often used as a reference source to remove the impact of precipitation on the other data measured at high frequencies. The SMAP wind data used in this article [24] are resampled on a 0.25° grid.

III. Surface Convective Wind Gust Estimation

This section presents two cases of the Sentinel-1, ASCAT-A/B/C, Windsat, and SMAP data collocation to observe surface wind patterns associated with deep convection. These cases can be considered as the representative ones of the LEO satellite data collocation to estimate convective wind gusts at mesoscales and submesoscales.

A. Mesoscale Squall Wind Pattern (Descending Case, February 4, 2019)

The first case (see Fig. 2) presents a mesoscale squall wind pattern based on the collocation of Sentinel-1, SMAP, Windsat, and ASCAT-A/B data offshore Angola, February 4, 2019. The observation time of the five devices for this region is presented in Table I. Fig. 2(a) shows a surface wind pattern observed by Sentinel-1 at 05:00:18–05:01:08 UTC. It spreads meridionally and zonally over nearly 2° (7.3°S-5.3°S, 8.5°E-10.5°E). The wind speed associated with this pattern is estimated from 12–25 m/s, as shown in [5]–[9]. The surface wind pattern in Fig. 2(a) has the shape of a squall line with a clear gust front.

Fig. 2(b) presents a surface wind pattern (12–18 m/s) observed by SMAP at 05:04 UTC. It spreads over the same zone as the Sentinel-1 wind pattern. Indeed, when the Sentinel-1 squall front is superimposed on Fig. 2(b), one may note that it corresponds to the wind front location observed by SMAP. This matching has been expected since the time lag between Sentinel-1 and SMAP is about 3 min. Likewise, some wind hot spots of Sentinel-1 and SMAP are closely located, although the SMAP wind intensity is lower than the Sentinel-1 one (18 m/s versus 25 m/s) due to the coarse SMAP data spatial resolution.

Fig. 2(c) illustrates a surface wind pattern (12–22 m/s) observed by Windsat (using the rain-free algorithm) at 05:24 UTC. It has the same extension as the Sentinel-1 and SMAP wind patterns. However, the Windsat one is at a different location. Indeed, by selecting a wind intensity threshold of 12 m/s, one can determine the front of the Windsat pattern as marked in Fig. 2(c). When the Sentinel-1 and SMAP wind front lines are superimposed on Fig. 2(c), one can note that they have a location shift of roughly 0.5° grid compared with the Windsat front line. Moreover, considering that the Windsat wind pattern occurs 20–23 min later than the Sentinel-1 and SMAP ones, it strengthens the assumption that the surface wind patterns observed on the Sentinel-1 and SMAP images at 05:01 and 05:04 UTC, respectively, move southwestwards. The velocity of wind pattern displacement (about 40 m/s) may be estimated by the distance (roughly 0.5° grid) and time (about 20–23 min) differences between Sentinel-1, SMAP, and Windsat. However, this method may not be sufficiently accurate, probably due to the spatial resolution gap between Sentinel-1, SMAP, and Windsat. The Doppler effect of satellite image acquisition may also contribute an error to calculate wind pattern displacement velocity. This calculation should be thus compared with the other sources (e.g., coastal radar) to verify and improve. Compared to SMAP, the intensity and shape of the wind pattern observed by Windsat are close to the Sentinel-1 ones, especially if comparing the strong wind intensity pixels.

Fig. 2(d) and (e) presents surface wind patterns observed by ASCAT-A and ASCAT-B at 08:10:40 and 09:18:56 UTC, respectively. The ASCAT wind intensity, especially the ASCAT-B one, is weaker than that of the Sentinel-1, SMAP, and Windsat in Fig. 2(a)–(c). Fig. 2(d) and (e) also compares the Sentinel-1, SMAP, and Windsat wind fronts with the ASCAT ones (assumed with a threshold of 8 m/s). As a result, one can note that the surface wind pattern observed on the Sentinel-1 image at 05:01 UTC [see Fig. 2(a)] moves southwestwards.

Surface wind patterns observed by Sentinel-1 and deep convective clouds detected by Meteosat have a strong relationship, as indicated in [5]–[9]. They are nearly at the same location, especially for the wind hot spots and the coldest cloud patterns. Likewise, the intensity of surface wind patterns corresponds to that of deep convective clouds. Fig. 3 presents the observation of deep convective clouds on Meteosat images (04:51:00–09:21:00 UTC) according to the Sentinel-1, SMAP, Windsat, and ASCAT-A/B data.

Fig. 3(a)–(c) shows deep convective clouds (200–230 K) observed by Meteosat corresponding to the surface wind patterns observed by Sentinel-1, SMAP, and Windsat. When the Sentinel-1, SMAP, Windsat wind fronts, and the Meteosat images are overlayed, one may note that surface wind patterns are located under the coldest cloud patterns (about 200 K) aloft. Likewise, when comparing Fig. 3(a)–(c), one notes that the deep convective cloud at 04:51 UTC moves southwestwards [observed by comparing Fig. 2(a)–(c)]. During 30 min (04:51–05:21 UTC), only the location of the coldest cloud pattern changes, whereas its shape remains the same. This corresponds to the observation of surface wind pattern evolution at 05:01, 05:04, and 05:24 UTC. However, when comparing Fig. 3(a)–(g) (04:51–07:36 UTC), one notes that from 05:21 UTC, both location and shape of the deep convective cloud have changed. Its displacement direction is not as evident as that from 04:51–05:21 UTC, and the extension and intensity of the coldest cloud pattern are reduced. Fig. 3(h) and (i) presents deep convective clouds (08:06 and 09:21 UTC) corresponding to the surface wind patterns observed by ASCAT-A/B (08:10:40 and 09:18:56 UTC). When the ASCAT-A/B wind fronts are placed on Fig. 3(h) and (i),

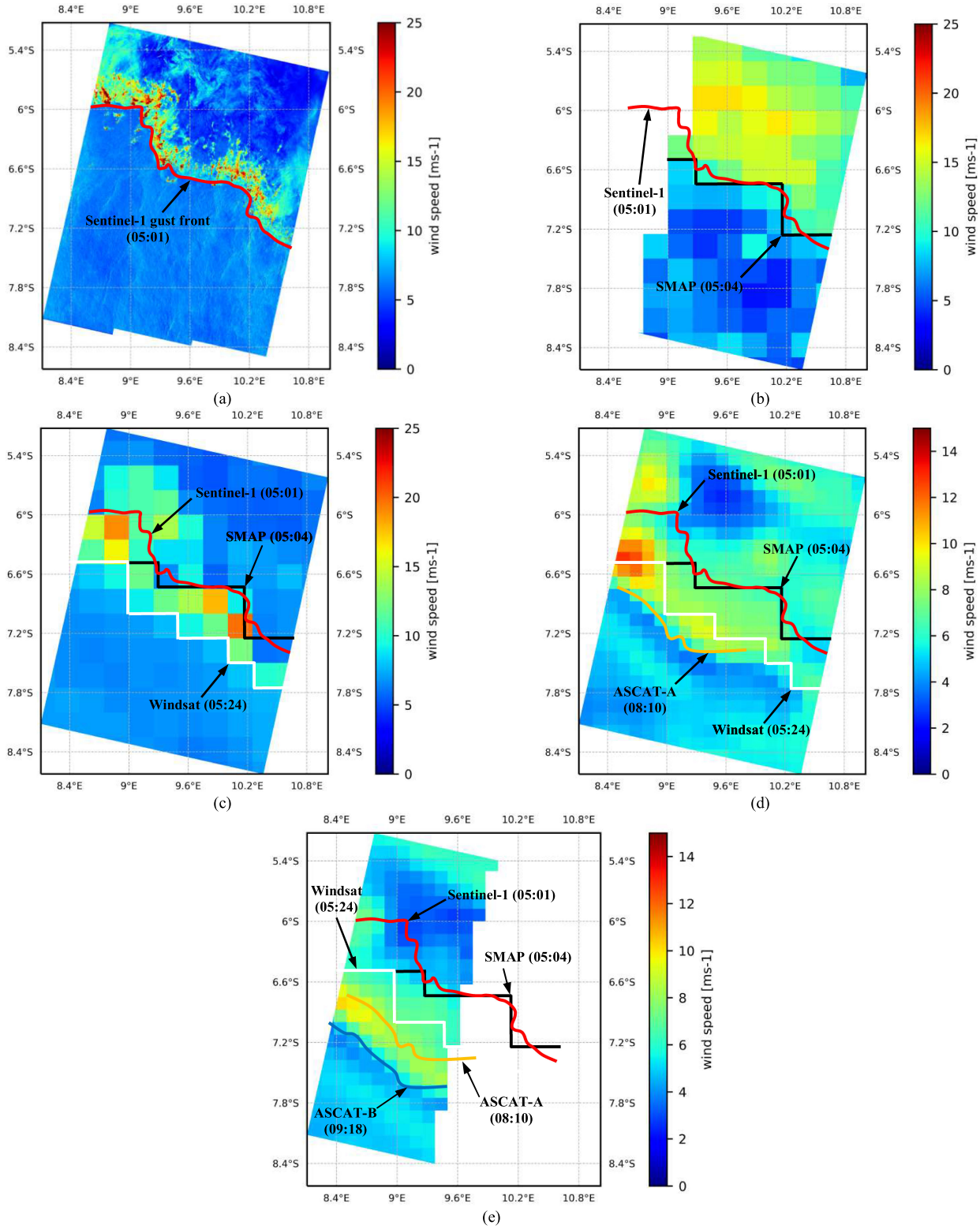

Fig. 2. Surface convective wind pattern in the shape of a mesoscale squall observed offshore Angola, February 4, 2019, by (a) Sentinel-1 *C*-band SAR at 05:00:18-05:01:08 UTC, (b) SMAP *L*-band Radiometer at 05:04 UTC, (c) Windsat *C*-, *X*-, and *K*-band Radiometer at 05:24 UTC, (d) ASCAT-A *C*-band Scatterometer at 08:10:40 UTC, and (e) ASCAT-B *C*-band Scatterometer at 09:18:56 UTC. The lines in red, black, white, yellow, and blue represent surface wind fronts assumed from Sentinel-1, SMAP, Windsat, ASCAT-A, and ASCAT-B data, respectively.

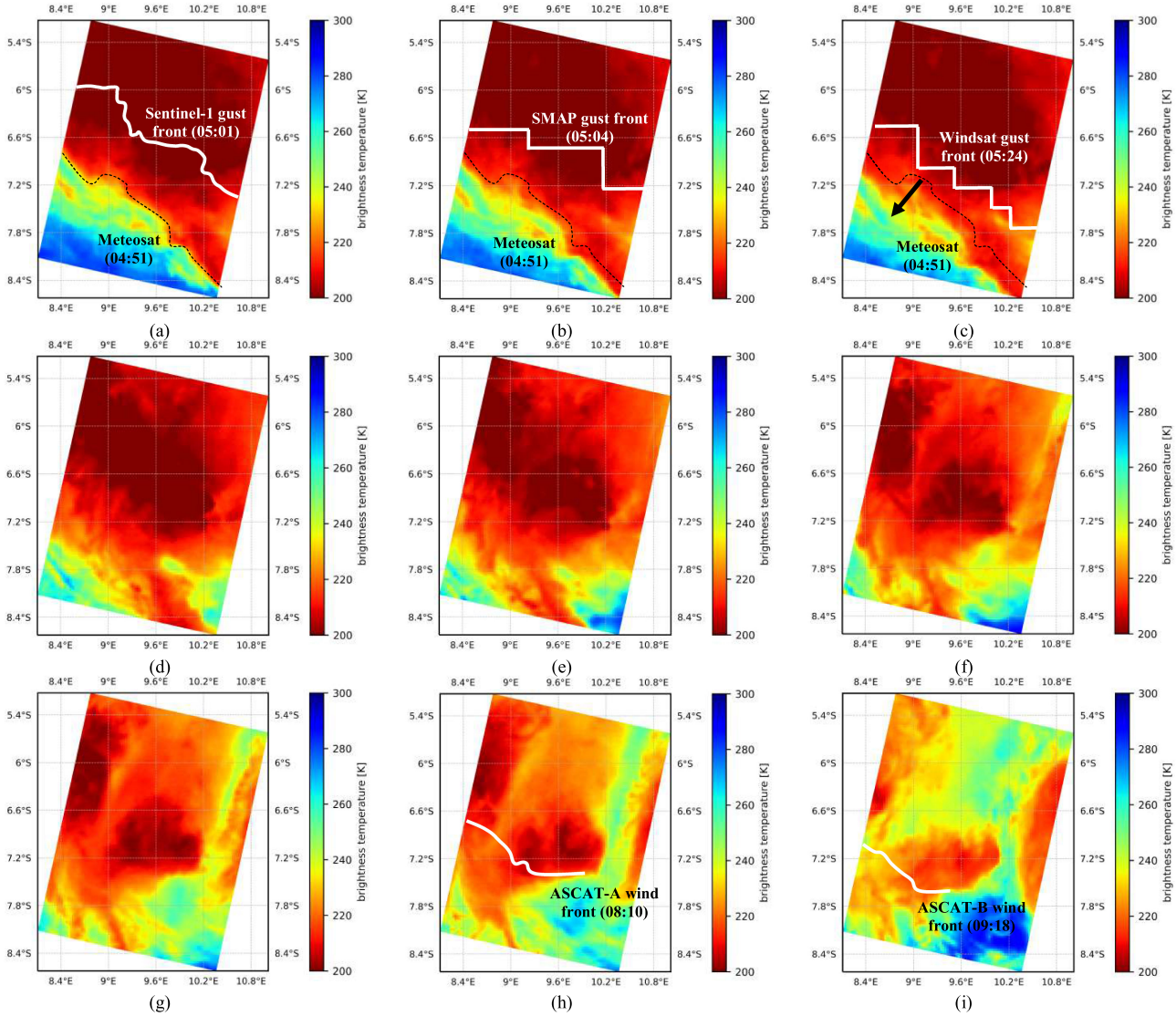

Fig. 3. (a)–(i) Deep convective clouds observed by Meteosat from 04:51 UTC to 09:21 UTC, February 4, 2019, corresponding to the surface convective wind patterns observed by Sentinel-1, SMAP, Windsat, ASCAT-A, and ASCAT-B. Fig. 3(a)–(c) (04:51, 05:06, and 05:21 UTC) corresponds to Fig. 2(a)–(c) (05:00:18-05:01:08, 05:04, and 05:24 UTC), respectively. Fig. 3(h) and (i) (08:06 and 09:21 UTC) corresponds to Fig. 2(d) and (e) (08:10:40 and 09:18:56), respectively. The white lines in Fig. 3(a)–(c) and 3(h) and (i) represent surface wind fronts assumed from Sentinel-1, SMAP, Windsat, ASCAT-A, and ASCAT-B data, respectively.

one notes that the surface wind patterns and the coldest cloud ones match in location. Likewise, the decrease in intensity of the coldest cloud patterns [Fig. 3(h) and (i)] corresponds to that of the ASCAT wind patterns [Fig. 2(d) and (e)], especially for the comparison between Fig. 2(e) and Fig. 3(i). This result illustrates (once again) the significant link between the intensity of deep convective clouds (through intense downdrafts) and that of surface wind patterns.

B. Submesoscale Convection Cell Wind Pattern (Ascending Case, December 19, 2019)

The second case (see Fig. 4) presents a submesoscale convection cell wind pattern based on the collocation of SMAP, Sentinel-1, Windsat, and ASCAT-A/C data offshore Ghana-Togo, December 19, 2019. The observation time of the five devices for this region is presented in Table I. Fig. 4(a) shows a surface wind pattern in the shape of a quasi-circle spreading over a roughly 0.5° grid observed by Sentinel-1 at 18:09:05–18:09:59 UTC. Fig. 4(b) illustrates a wind pattern observed by SMAP at 17:47 UTC, 22 min earlier than the Sentinel-1 wind pattern observation. Imposing a threshold of 10–12 m/s wind intensity, Fig. 4(b) exhibits that the SMAP and Sentinel-1 wind patterns match in horizontal extension (about 0.5° grid) at the same location. It leads to an assumption that the surface wind pattern observed on Sentinel-1 images [see Fig. 4(a)] has moved very slowly for 23 min. Fig. 4(c) presents a surface wind pattern observed by Windsat at 18:12 UTC, 3 and 26 min later compared to the observation of the Sentinel-1 and SMAP wind patterns, respectively. The Windsat wind pattern

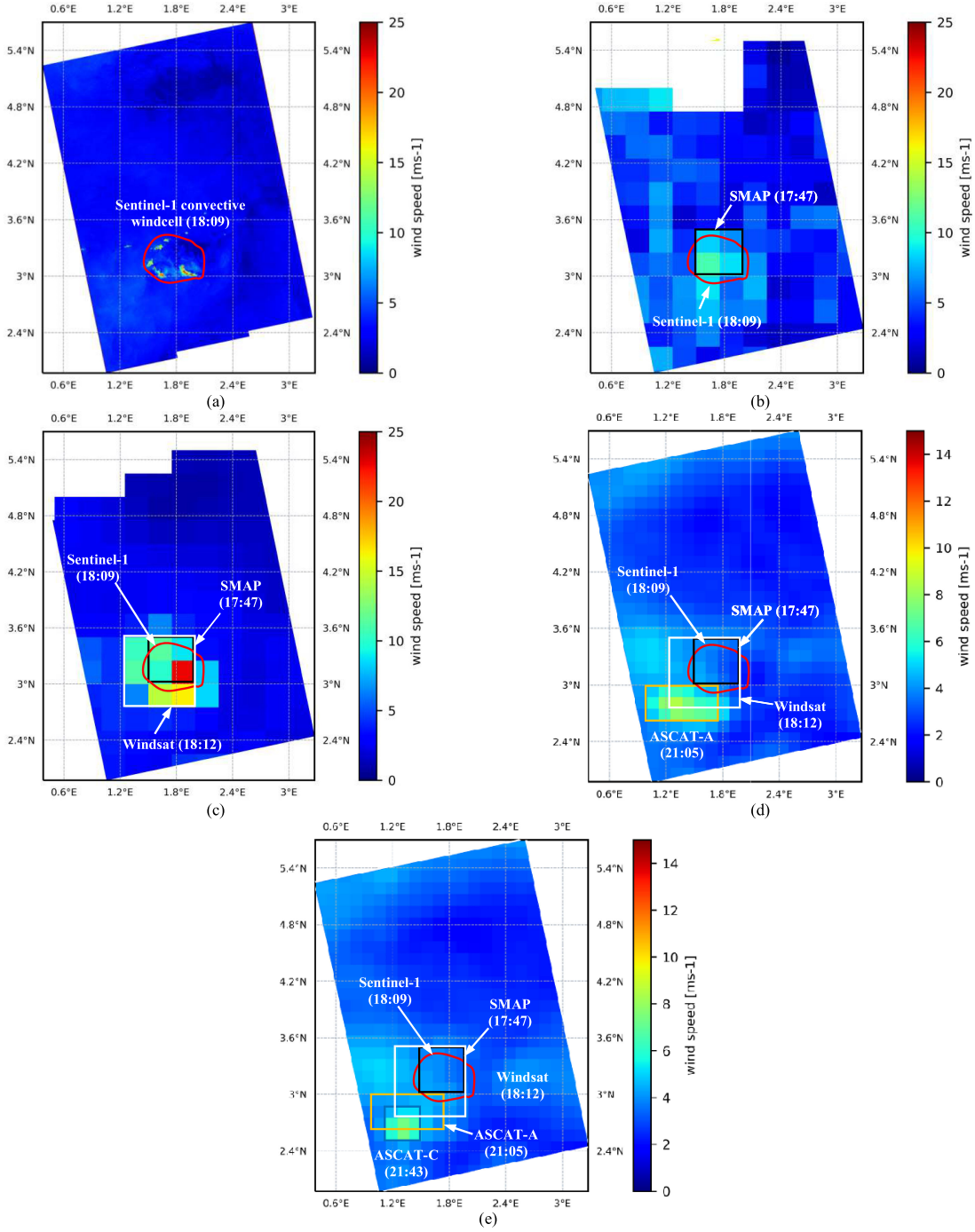

Fig. 4. Surface convective wind pattern in the shape of a convection cell observed offshore Ghana-Togo, December 19, 2019, by (a) Sentinel-1 *C*-band SAR at 18:09:05-18:09:59 UTC, (b) SMAP *L*-band radiometer at 17:47 UTC, (c) Windsat *C*-, *X*-, and *K*-band radiometer at 18:12 UTC, (d) ASCAT-A *C*-band scatterometer at 21:05:04 UTC, and (e) ASCAT-C *C*-band scatterometer at 21:43:28 UTC. The circle/rectangles in red, black, white, yellow, and blue represent surface wind cells assumed from Sentinel-1, SMAP, Windsat, ASCAT-A, and ASCAT-C data, respectively.

intensity (12–22 m/s) is close to the Sentinel-1 one and higher than the SMAP one. In particular, the Windsat wind hot spot of 22 m/s (3°N–3.25°N, 1.75°E–2°E) is located at the same coordinate as the Sentinel-1 one. Selecting a threshold of 12 m/s and overlaying the Sentinel-1 and SMAP wind cells on Fig. 4(c), one can note that the Windsat wind pattern has a close location to the others. The low location shift is due to the SMAP and Windsat coarse spatial resolutions (0.25° grid).

Fig. 4(d) and (e) shows surface wind patterns observed by ASCAT-A and ASCAT-C at 21:05:04 and 21:43:28 UTC, thus about 3 h and 3.5 h later than the Sentinel-1 wind pattern observation, respectively. The ASCAT-A/C wind pattern intensity (about 8–9 m/s) is lower than the Sentinel-1 and Windsat ones. Likewise, their horizontal extension is narrower. Overlaying the Sentinel-1, SMAP, Windsat wind cells on Fig. 4(d) and (e), one notes that the surface wind pattern moves southwestwards.

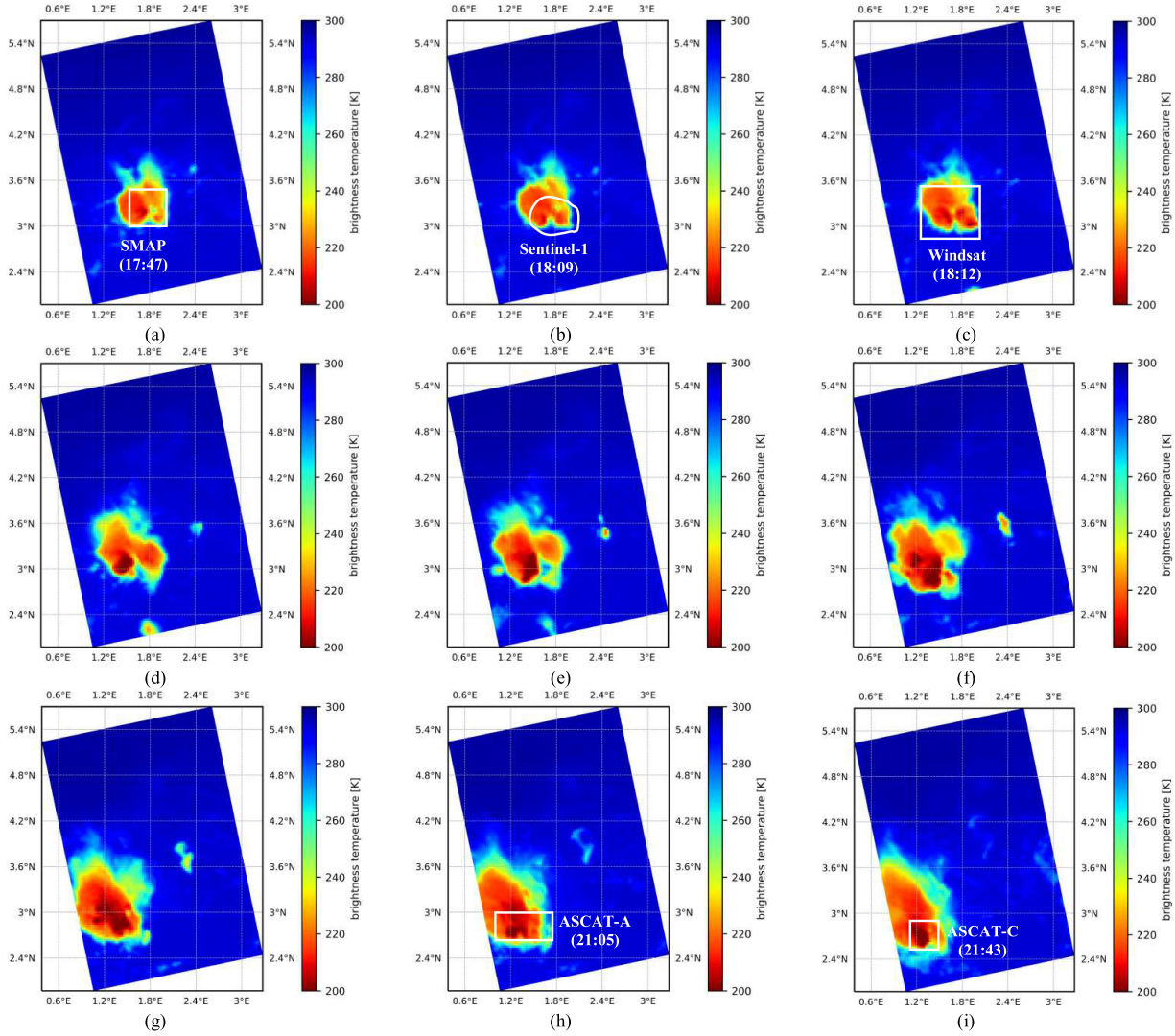

Fig. 5. (a)–(i) Deep convective clouds in the shape of a convection cell observed by Meteosat from 17:51:00 UTC to 21:36:00 UTC, December 19, 2019, corresponding to the surface convective wind patterns observed by SMAP, Sentinel-1, Windsat, ASCAT-A, and ASCAT-C. Fig. 5(a)–(c) (17:51:00, 18:06:00, and 18:21:00 UTC) corresponds to Fig. 4(a)–(c) (17:47:00, 18:09:05-18:09:59, and 18:12:00 UTC), respectively. Fig. 5(h) and (i) (21:06:00 and 21:36:00 UTC) corresponds to Fig. 4(d) and (e) (21:05:04 and 21:43:28 UTC), respectively. The white circle/rectangles in Fig. 5(a)–(c) and 5(h) and (i) represent surface wind cells assumed from SMAP, Sentinel-1, Windsat, ASCAT-A, and ASCAT-C data, respectively.

When comparing the location of this wind cell in Fig. 4(a)–(e), one can see that it has been moving slowly for more than 3 h.

Fig. 5 illustrates the observation of deep convective clouds by Meteosat (17:51:00–21:36:00 UTC) corresponding to the surface wind patterns in Fig. 4(a)–(e). Fig. 5(a)–(c) (17:51:00, 18:06:00, and 18:21:00 UTC) corresponds in location and observation time to the SMAP (17:47:00 UTC), Sentinel-1 (18:09:05-18:09:59 UTC), and Windsat images (18:12:00 UTC), respectively. The SMAP, Sentinel-1, and Windsat wind cells correspond to the location of the coldest cloud patterns (about 220 K) observed by Meteosat. From 17:51:00 to 18:21:00 UTC, the deep convective cloud moves slowly southwestwards. This observation corresponds to the slow displacement of the surface wind pattern observed from 17:47:00 to 18:12:00 UTC [see Fig. 4(a)–(c)]. From 18:21:00 to 21:36:00 UTC, the deep convective cloud is moving southwestwards. The cloud displacement corresponds to the surface wind patterns observed by ASCAT-A/C from 18:12:00 to 21:43:28 UTC. Likewise, the ASCAT-A/C wind cells [Fig. 4(d) and (e)] with high wind intensity (about 8–9 m/s) correspond to the coldest cloud pattern locations [Fig. 5(h) and (i)].

IV. Relationship Between Surface Wind Pattern and Precipitation

In addition to the BT measurements and then surface wind speed retrieval, the Windsat Radiometer can measure the corresponding rainfall. This brings relevant information to study the relationship between surface wind patterns and precipitation under deep convection. Through this work, one may more clearly understand that the high-intensity radar backscattering areas observed on the *C*-band SAR images are associated with surface wind gusts or precipitation.

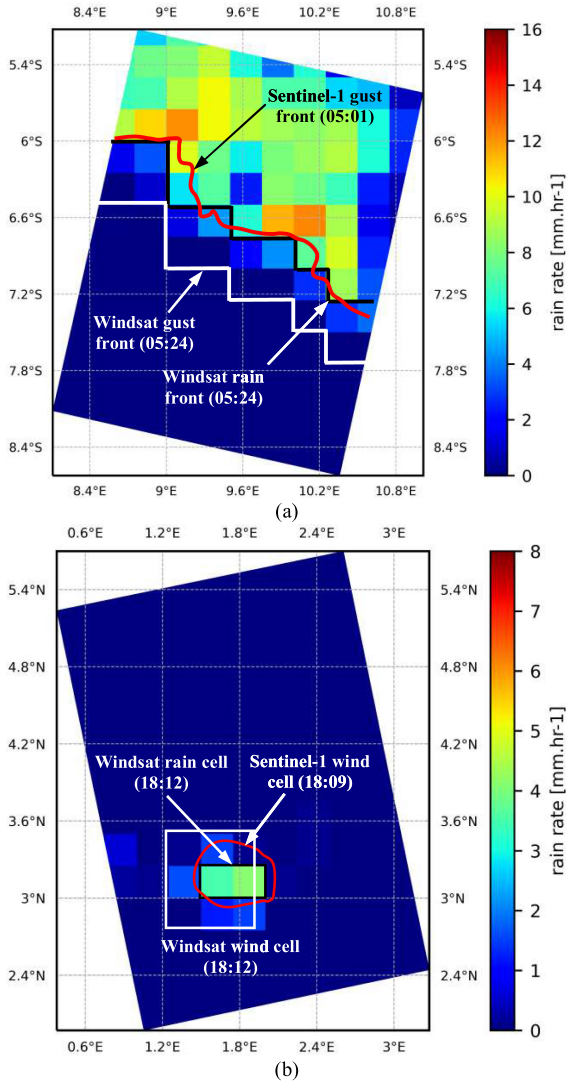

Fig. 6. Convective rainfall measured by the Windsat Radiometer corresponding to the surface wind patterns observed by Sentinel-1 and Windsat. (a) February 4, 2019, 05:24:00 UTC. (b) December 19, 2019, 18:12:00 UTC. The rectangles/circular in red, white, and black represent surface wind fronts assumed from Sentinel-1 and Windsat data and rain front from Windsat data, respectively.

Fig. 6 presents the rainfall measured by Windsat corresponding to the Sentinel-1 and Windsat wind patterns. The Sentinel-1 and Windsat wind fronts are superimposed on Fig. 6. Fig. 6(a) shows that the Windsat precipitation illustrates a squall line like the Sentinel-1 and Windsat surface wind patterns in Fig. 2(a) and (c), respectively. Some heavy rainfall (9–13 mm/h) corresponds in location to the high-intensity winds; however, there is a significant location shift (roughly 0.5° grid) between the Windsat wind and rain fronts. Note that both events are observed at the same time (05:24:00 UTC). Therefore, it indicates that surface convective wind gust occurs before the convective precipitation. Likewise, when the Sentinel-1 wind front at 05:00:18-05:01:08 UTC is overlayed on Fig. 6(a), one notes that it is located at the same place as the Windsat rain front observed at 05:24:00 UTC. This result indicates that the high-intensity radar backscattering on the Sentinel-1 image is not associated with precipitation since the latter occurs 23 min later than the Sentinel-1 observation time (05:00:18-05:01:08 UTC). In other words, the high-intensity NRCS observed on the Sentinel-1 image must be related to convective wind gusts rather than precipitation.

Fig. 6(b) shows the Windsat rain cell corresponding to the Sentinel-1 and Windsat wind cells in Fig. 4(a) and (c). The rainfall intensity (about 3–4 mm/h) is much lower than the one shown in Fig. 6(a). Due to the Windsat coarse spatial resolution, it is hard to observe the location shift between the Windsat wind and rain cells. However, one can note that the Windsat wind cell tends to move southwestwards compared to the Windsat rain cell. The Sentinel-1 wind cell (18:09:05-18:09:59 UTC) overlayed on Fig. 6(b) illustrates that it is at the same location as the Windsat rain cell (18:12 UTC), whereas the latter is observed 3 min later. As well as Fig. 6(a), this result indicates that the high-intensity radar backscattering observed on the Sentinel-1 image is associated with surface convective wind pattern.

V. Conclusion

This article presented two cases showing the observation of surface wind patterns generated by deep convection using the collocation of several LEO satellite data, including Sentinel-1 *C*-band SAR, ASCAT-A/B/C scatterometers, Windsat *C*-, *X*-, and *K*-band radiometer, and SMAP *L*-band radiometer. The first case (February 4, 2019) showed a mesoscale surface convective wind pattern (a squall line), whereas the second case (December 19, 2019) illustrated a submesoscale convection cell wind pattern. For the two cases, this study indicated that the collocation of data from the five LEO satellites is a relevant methodology to 1) observe surface winds under CSs at various scales (mesoscales and submesoscales) and 2) exhibit the space and time evolution of surface convective wind patterns at various scales.

Likewise, this study showed that the Sentinel-1 SAR images with a high spatial resolution and wide swath can be used for observing not only convective wind patterns at various scales but also wind hot spots at a small scale. The scatterometers (ASCAT-A/B/C) and radiometers (Windsat and SMAP) data with a coarser spatial resolution but a larger swath can observe mesoscale and submesoscale convective wind patterns larger than 0.25° grid. Among the scatterometers and radiometers, the Windsat rain-free data can estimate more accurately surface wind speed, compared to the one retrieved from Sentinel-1 data [Fig. 2(a) versus (c), Fig. 4(a) versus (c)], especially for wind hot spots.

The observation time lag between Sentinel-1, SMAP, and Windsat over the Gulf of Guinea is short compared to the one between ASCAT-A/B/C. Therefore, the Sentinel-1, SMAP, and Windsat data collocation, as shown in Figs. 2 and 4, leads to observing the short-term changes of surface wind patterns, whereas that of the Sentinel-1, SMAP, Windsat, and ASCAT data brings a longer term observation of the wind pattern evolution. The Meteosat images collocated with the LEO data in Figs. 3 and 5 indicated that the changes of surface wind patterns, including displacement and the intensity variability of wind hot spots, are associated with convection cloud variability. Indeed, the surface wind pattern moves according to the deep convective clouds, and the wind intensity corresponds to the BT one.

The Windsat radiometer can measure BT to retrieve surface wind speed and rainfall. This ability facilitates the study of the relationship between surface wind patterns and precipitation under CSs. In particular, it provided elements to investigate whether the high-intensity radar backscattering observed on the *C*-band SAR images (Sentinel-1, Radarsat-2, Envisat) is associated with strong surface winds and/or rain. The results in Fig. 6 strengthened the observations underlined in [5]–[9] that the high-intensity NRCS on Sentinel-1 images is associated with surface convective wind gusts, in agreement with the results obtained in [14] and [15]. The *C*-band radar backscattering is thus much less impacted by precipitation compared to surface winds, and its effect should be negligible for the retrieval of surface wind speed above 7 m/s. Likewise, the study based on the *C*-band ASCAT data [18] assumed that the rain impact is weak for surface wind speed retrieval.

As well as surface wind patterns, the assumption of a relationship between convective precipitation and deep convective cloud is reasonable. The comparisons between Figs. 3(c) and 6(a) and between Figs. 5(c) and 6(b) showed that the two features possibly match in intensity; however, they may have a difference in location and observation time. Due to the coarse spatial resolution of the Windsat rainfall data, it is hard to clarify here whether the convective rainfall hot spots correspond to the coldest cloud patterns as shown between the latter and strong surface winds. A deeper study with more cases should be carried out to understand the relationship between precipitation, strong surface winds, and deep convective clouds. Such a study is significant to estimate convective rainfall intensity, then forecast flash floods.

The short- and long-term observations of sea surface wind patterns under deep convection based on the collocation of various satellites and the strong relationship between strong surface winds and deep convective clouds bring a significant perspective for the forecast of convective wind gusts. This work can be performed by using artificial intelligence (AI) combined with GEO images as input data. The remote sensing data (Sentinel-1 SAR, ASCAT-A/B/C, Windsat, and SMAP) are used as training and validating data for the AI models.

Acknowledgment

The Sentinel-1A/B images are given by the European Copernicus Program. The ASCAT-A/B/C data are downloaded from.[1] The Windsat and SMAP data are offered by.[2] Meteosat images are provided by the European Organization for the Exploitation of Meteorological Satellites (EUMETSAT) via EUMETSAT Data Center. The authors would like to thank the Editors and Reviewers for the valuable comments.

References

[1] W. Thiery *et al.*, "Hazardous thunderstorm intensification over Lake Victoria," *Nature Commun.*, vol. 7, 2016, Art. no. 12786, doi: 10.1038/ncomms12786.

[2] J. M. Chamberlain, C. L. Bain, D. F. A. Boyd, K. McCourt, T. Butcher, and S. Palmer, "Forecasting storms over Lake Victoria using a high resolution model," *Meteorol. Appl.*, vol. 21, no. 2, pp. 419–430, Apr. 2014, doi: 10.1002/met.1403.

[3] S. J. Kastman, S. P.Market, I. N. Fox, A. L. Foscato, and R. A. Lupo, "Lightning and rainfall characteristics in elevated vs. Surface based convection in the Midwest that produce heavy rainfall," *Atmosphere*, vol. 8, no. 2, Feb. 2017, Art. no. 36, doi: 10.3390/atmos8020036.

[4] V. Mathon and H. Laurent, "Life cycle of Sahelian mesoscale convective cloud systems," *Quart. J. Roy. Meteorol. Soc.*, vol. 127, pp. 377–406, 2001, doi: 10.1002/qj.49712757208.

[5] T. V. La, C. Messager, M. Honnorat, and C. Channelliere, "Detection of convective systems through surface wind gust estimation based on Sentinel-1 images: A new approach," *Atmos. Sci. Lett.*, vol. 19, no. 7, Dec. 2018, Art. no. e863, doi: 10.1002/asl.863.

[6] T. V. La and C. Messager, "Convective system sea surface wind pattern detection and variability observation from a combination of Sentinel-1 and Radarsat-2 images," *Remote Sens. Lett.*, vol. 11, no. 5, pp. 446–454, Feb. 2020, doi: 10.1080/2150704X.2020.1731621.

[7] T. V. La *et al.*, "Use of Sentinel-1 C-band SAR images for convective system surface wind pattern detection," *J. Appl. Meteorol. Climatol.*, vol. 59, no. 8, pp. 1321–1332, Aug. 2020, doi: 10.1175/JAMC-D-20-0008.1.

[8] T. V. La and C. Messager, "Convective system dynamics viewed in 3D over the oceans," *Geophys. Res. Lett.*, vol. 48, Mar. 2021, Art. no. e2021GL092397, doi: 10.1029/2021GL092397.

[9] T. V. La and C. Messager, "Convective system observations by LEO and GEO satellites in combination," *IEEE J. Sel. Topics Appl. Earth Observ. Remote Sens.*, vol. 14, pp. 11814–11823, Nov. 2021, doi: 10.1109/JSTARS.2021.3127401.

[10] E. L. Kuchera and M. D. Parker, "Severe convective wind environments," *Weather Forecasting*, vol. 21, no. 4, pp. 595–612, Aug. 2006, doi: 10.1175/WAF931.1.

[11] P. F. Waniha, R. D. Roberts, J. W. Wilson, A. Kijazi, and B. Katole, "Dual-polarization radar observations of deep convection over Lake Victoria basin in East Africa," *Atmosphere*, vol. 10, no. 11, Nov. 2019, Art. no. 706, doi: 10.3390/atmos10110706.

[12] M. J. Kaiser, "The impact of extreme weather on offshore production in the Gulf of Mexico," *Appl. Math. Model.*, vol. 32, no. 10, pp. 1996–2018, 2008, doi: 10.1016/j.apm.2007.06.031.

[13] M. Hareland and C. Price, "Thunderstorm trends over Africa," *J. Climate*, vol. 33, no. 7, pp. 2741–2755, 2020, doi: 10.1175/JCLI-D-18-0781.1.

[14] R. F. Contreras and W. J. Plant, "Surface effect of rain on microwave backscatter from the ocean: Measurements and modeling," *J. Geophys. Res.*, vol. 111, no. C8, Aug. 2006, Art. no. C08019, doi: 10.1029/2005JC003356.

[15] F. Xu, X. Li, P. Wang, J. Yang, W. G. Pichel, and Y. Q. Jin, "A backscattering model of rainfall over rough sea surface for synthetic aperture radar," *IEEE Trans. Geosci. Remote Sens.*, vol. 53, no. 6, pp. 3042–3054, Jun. 2015.

[16] T. J. Kilpatrick and S.-P. Xie, "ASCAT observations of downdrafts from mesoscale convective systems," *Geophys. Res. Lett.*, vol. 42, no. 6, pp. 1951–1958, Mar. 2015, doi: 10.1002/2015GL063025.

[17] G. Priftis, T. J. Lang, and T. Chronis, "Combining ASCAT and NEXRAD retrieval analysis to explore wind features of mesoscale oceanic systems," *J. Geophys. Res., Atmos.*, vol. 123, no. 18, pp. 10341–10360, Sep. 2018, doi: 10.1029/2017JD028137.

[18] Z. Wang *et al.*, "Scatterometer sea surface wind product validation for HY-2C," *IEEE J. Sel. Topics Appl. Earth Observ. Remote Sens.*, vol. 14, pp. 6156–6164, Jun. 2021, doi: 10.1109/JSTARS.2021.3087742.

[19] W. Lin, M. Portabella, A. Stoffelen, A. Verhoef, and A. Turiel, "ASCAT wind quality control near rain," *IEEE Trans. Geosci. Remote Sens.*, vol. 53, no. 8, pp. 4165–4177, Aug. 2015.

[20] W. Lin, M. Portabella, A. Stoffelen, J. Vogelzang, and A. Verhoef, "ASCAT wind quality under high subcell wind variability conditions," *J. Geophys. Res., Oceans*, vol. 120, pp. 5804–5819, 2015, doi: 10.1002/2015JC010861.

[21] T. Meissner and F. J. Onentz, "Wind-vector retrievals under rain with passive satellite microwave radiometers," *IEEE Trans. Geosci. Remote Sens.*, vol. 47, no. 9, pp. 3065–3083, Sep. 2009.

[22] Remote Sensing Systems, Aug. 2021. [Online]. Available: https://www.remss.com/missions/windsat

[23] T. Meissner, L. Ricciardulli, and F. J.Onentz, "Capability of the SMAP mission to measure ocean surface winds in storms," *Bull. Amer. Meteorol. Soc.*, vol. 98, no. 8, pp. 1660–1677, Aug. 2017, doi: 10.1175/BAMS-D-16-0052.1.

[1][Online]. Available: https://osi-saf.eumetsat.int

[2][Online]. Available: www.remss.com/

[24] Remote Sensing Systems, Aug. 2021. [Online]. Available: https://www.remss.com/missions/smap/winds

[25] C. Nie and D. G. Long, "A C-band wind/rain backscatter model," *IEEE Trans. Geosci. Remote Sens.*, vol. 45, no. 3, pp. 621–631, Mar. 2007.

[26] W. Alpers, Y. Zhao, A. A. Mouche, and P. W. Chan, "A note on radar signatures of hydrometeors in the melting layer as inferred from Sentinel-1 SAR data acquired over the ocean," *Remote Sens. Environ.*, vol. 253, Feb. 2021, Art. no. 112177, doi: 10.1016/j.rse.2020.112177.

[27] R. Roca, T. Fiolleau, and D. Bouniol, "A simple model of the life cycle of mesoscale convective systems cloud shield in the tropics," *J. Climate*, vol. 30, no. 11, pp. 4283–4298, Jun. 2017, doi: 10.1175/JCLI-D-16-0556.1.

[28] J. Verspeek, A. Stoffelen, M. Portabella, H. Bonekamp, C. Anderson, and J. Figa Saldaña, "Validation and calibration of ASCAT using CMOD5.n," *IEEE Trans. Geosci. Remote Sens.*, vol. 48, no. 1, pp. 386–395, Jan. 2010.

[29] T. V. La, A. Khenchaf, F. Comblet, and C. Nahum, "Exploitation of C-band Sentinel-1 images for high-resolution wind field retrieval in coastal zones (Iroise coast, France)," *IEEE J. Sel. Topics Appl. Earth Observ. Remote Sens.*, vol. 10, no. 12, pp. 5458–5471, Dec. 2017.

[30] T. V. La, A. Khenchaf, F. Comblet, and C. Nahum, "Assessment of wind speed estimation from C-band Sentinel-1 images using empirical and electromagnetic models," *IEEE Trans. Geosci. Remote Sens.*, vol. 56, no. 7, pp. 4075–4087, Jul. 2018.

[31] W. R. Cotton, G. Bryan, and S. C. van den Heever, "Storm and cloud dynamics—The dynamics of clouds and precipitating mesoscale systems, Chapter 9—mesoscale convective systems," *Int. Geophys.*, vol. 99, pp. 455–526, 2011.

[32] M. Imberger, X. G. Larsén, and N. Davis, "Investigation of spatial and temporal wind-speed variability during open cellular convection with the model for prediction across scales in comparison with measurements," *Boundary-Layer Meteorol.,* vol. 179, pp. 291–312, 2021, doi: 10.1007/s10546-020-00591-0.

[33] OSI SAF, Observing Oceans From Space, Aug. 2021. [Online]. Available: https://osi-saf.eumetsat.int